



Near Real Time Satellite Event Detection, Characterization, and Operational Assessment Via the Exploitation of Remote Photoacoustic Signatures

Justin Spurbeck, et al. [full author details at the end of the article]

Accepted: 18 January 2021 / Published online: 13 April 2021

© The Author(s) 2021

Abstract

Current active satellite maneuver detection techniques can resolve maneuvers as quickly as fifteen minutes post maneuver for large Δv when using angles-only optical tracking. Medium to small magnitude burn detection times range from 6 to 24 h or more. Small magnitude burns may be indistinguishable from natural perturbative effects if passive techniques are employed. Utilizing a photoacoustic signature detection scheme can allow for near real time maneuver detection and spacecraft parameter estimation. We define the acquisition of hypertemporal photometric data as photoacoustic sensing because the data can be played back as an acoustic signal. Studying the operational frequency spectra, profile, and aural perception of an active satellite event such as a thruster ignition or any subsystem operation can provide unique signature identifiers that support resident space object characterization efforts. A thruster ignition induces vibrations in a satellite body which can modulate reflected sunlight. If the reflected photon flux is sampled at a sufficient rate, the change in light intensity due to the propulsive event can be detected. Sensing vibrational mode changes allows for a direct timestamp of thruster ignition and shut-off events and thus makes possible the near real time estimation of spacecraft Δv and maneuver type if coupled with active observations immediately post maneuver. This research also investigates the estimation of other impulse related spacecraft parameters such as mass, specific impulse, exhaust velocity, and mass flow rate using impulse-momentum and work-energy methods. Experimental results to date have not yet demonstrated an operator-correlated detection of a propulsive event; however, the application of photoacoustic sensing has exhibited characteristics unique to hypertemporal photometry that are discussed alongside potential improvements to increase the probability of active satellite event detection. Simulations herein suggest that large, potentially destructive modal displacements are required for optical sensor detection and thus more comprehensive vibration modeling and signal-to-noise ratio improvements should be explored.

Advanced Maui Optical and Space Surveillance Technologies (AMOS 2018 & 2019)
Guest Editors: James M. Frith, Lauchie Scott, Islam Hussein

An earlier version of this article was first presented at the 19th Advanced Maui Optical and Space Surveillance Technologies Conference, held in Wailea, Maui, Hawaii, September 11–14, 2018

Keywords Photoacoustic sensing · Spacecraft parameter estimation · Hypertemporal photometric data · Maneuver detection · Astrodynamics · Orbit determination · Satellite characterization · Space situational awareness

Introduction

The space environment near Earth has grown crowded since the dawn of the space age in the late 1950s. Technological advances and decreases in manufacturing costs have led to a significant increase in the space object population. Increased launch frequency by government agencies and the private sector coupled with the growing number of uniquely controlled payloads that can be included per launch demonstrate the need for a robust system to monitor and protect each near-Earth orbital regime.

A challenge inherent to the crowded space environment is how to effectively predict Resident Space Object (RSO) collision risks and use that information to ensure active satellite survival and compliance with the Inter-Agency Space Debris Coordination Committee guidelines [1]. The 18th Space Control Squadron (18 SPCS) at the Combined Space Operations Center provides conjunction data messages via a global array of sensors to operators with assets that have secondary RSOs within their screening volume. Operators will use this information to maneuver their assets into a safer orbit if required. Some operators will send a predicted ephemeris including the planned maneuver to the 18 SPCS such that they can preemptively screen it against any other secondary RSOs. The screening is to ensure the maneuver does not put the satellite into the path of another object, effectively defeating the purpose of the collision avoidance maneuver in the first place. There are, however, instances where an operator does not follow this procedure or an unexpected dynamic event occurs, and thus maneuvers and potential conjunctions are unpredictable. This scenario demonstrates the need for a method to quickly detect when an uncooperative RSO has maneuvered and estimate its new trajectory. If there were such a method, it would not only help reduce potential conjunction risks much sooner, it would also provide data that would allow satellite operational capability assessments.

In addition to the need for near real time monitoring of active satellites, there are still gaps in how both active and inactive RSOs are characterized and uniquely identified. Any source of data that would provide unique signature identifiers based on RSO shape, behavior, mass, or other parameter increases our ability to better understand the RSO population. Thus, this research presents a new method to detect satellite maneuvers in near real time and extends the method to support RSO characterization and spacecraft parameter estimation.

Photoacoustic Sensing and Characterization

A noteworthy phenomenon becomes observable if photometric data is collected at a rate above 40 kHz. The human ear is capable of discerning frequencies from 20 Hz to 20 kHz. Thus, an acoustic signal can be generated from hypertemporal photometric data by converting the frequency content within a light curve to audio. To abide by the Nyquist Theorem, sampling at 40 kHz plus a safety margin would recover all naturally

discernable sound. We define the acoustic playback of high-rate photometric data as its photoacoustic signature. The light to sound conversion is possible because photons carry an equivalent information content that an acoustic wave cannot because there is no medium for it to propagate through in the vacuum of space [2, 3]. This technique has been proven robust in terrestrial tests that demonstrated the capability to accurately recover a conversation or song on the radio by collecting the light being modulated by a flexible surface nearby the acoustic source such as a plant leaf [4]. The direct analogy to applying photoacoustic sensing remotely is to imagine a satellite's solar array as the leaf in the prior example and a thruster ignition event as the acoustic source from the radio.

An example of how an acoustic interpretation of an inherently non-acoustic signal supported the characterization of a physical event is seen in the analysis of plasma wave data from the Voyager 1 spacecraft. NASA mission scientists converted the vibrations of dense ionized gas detected by the spacecraft's plasma wave instrument into an acoustic signal. While listening to the acoustic playback, the mission scientists noticed a rising tone which helped infer a continuously increasing density profile, detection of interstellar plasma, transit of the heliopause, and thus a departure from our Solar System [5]. The aural perception of similar RSO events may be one modality used to characterize satellites in a manner similar to how biometric recognition systems operate. Organizing RSO photometric event signal information into its unique frequency content, transients, pitch, aural perception, dead zones, harmonics, power level, profile, and other categories could provide the modalities needed to implement an RSO recognition system. These modalities would fulfill the universality, distinctiveness, permanence, and collectability requirements for such a system [6, 7]. Fusing these modalities with other known or inferred spacecraft parameters could yield the equivalent of an n-factor authentication system that identifies and characterizes RSOs.

Resident Space Object Event Detection

The prior section discussed the potential for RSO event characterization and identification via acoustic interpretation of remote photoacoustic signatures obtained from active satellite observations. The satellite events assumed detection through either direct thruster plume observations for maneuvers, subtle changes detected in the hypertemporal photometric data frequency content due to an on-board event, or a combination of the two. This section will define specifics of the event recognition techniques from a satellite vibration mode change detection standpoint, focusing primarily on maneuvers. While the focus remains on propulsive events, these techniques could readily be applied to collision, explosive, or disintegration events, thermal snap, and abrupt changes in the space environment.

Methods to detect unmodeled dynamic events are often passive techniques that use an algorithm to sample historical ephemeris data and apply statistical methods until it can suggest an object's trajectory has deliberately shifted. Assuming an unmodeled dynamic event is a maneuver and depending on the magnitude of the burn, this sort of event detection can take anywhere from around ninety minutes up to several days to resolve. If the burn is small enough, it may be indistinguishable from the natural perturbative effects [8]. Large maneuvers may cause a complete loss of an object's

trajectory and can be tedious to reacquire. An active detection technique for a Geosynchronous Earth Orbit (GEO) satellite using ground based optical tracking and sequential estimation tools showed that a Δv of 1.0 m/s could be detected as soon as fifteen minutes after a maneuver while a Δv of 0.01 m/s could take 12–24 h to discern with confidence [9]. Another promising event detection example is demonstrated in publicly available footage from ExoAnalytics which captures thruster plumes in the geosynchronous regime.¹

Maneuver Detection

Collecting hypertemporal photometric data on an active satellite has the potential to detect and characterize on-board operational events in near real time. It is assumed that the ignition and nominal operation of a thruster imparts energy into a satellite body. This energy may induce vibration in flexible components depending on the geometry, material, and inertial properties of the satellite. If any of these structures have reflective surfaces, the reflected photon flux will be modulated by the induced vibration. Further, if the relative displacement of the reflective surfaces is large enough, it should be possible to detect the change in outgoing photon flux with an optical telescope.

Synthetic Light Curve Simulation To demonstrate an event detection in this manner, a 2 kHz synthetic light curve is simulated for an active satellite with a nadir aligned, velocity constrained attitude profile in GEO assuming the basic box-wing structural model in Fig. 1 and a simplified Cook-Torrance reflectance model [10]. The light curve model was modified to operate on a flat-plate surface and relies on both diffuse and spectral bidirectional reflectance distribution functions, incidence angles, and reflected intensity values. To calculate the apparent visual magnitude as measured by an observer, the following formula can be implemented:

$$m_{v,object} = m_{v,sun} - 2.5 \log_{10} \left(\sum_{i=1}^{N_{facets}} \frac{S_i}{4\pi\rho_d^2} \right) + N(\mu, \sigma_{v,atm}^2) \quad (1)$$

where $m_{v,sun}$ is the apparent visual magnitude of the sun, ρ_d is the distance between the observer and RSO, N_{facets} is the number of facets of the box-wing model, and the sum term denotes the effect from each given facet, further defined in Eq. (2). The last term in Eq. (1) represents the additive effect of atmospheric scintillation defined as a Gaussian distribution with mean μ and $\sigma_{v,atm}^2$ representing its variance. Unless explicitly stated otherwise, a 0.04 m_v standard deviation and zero mean are assumed for the noise distribution, also denoted as $N(0, 0.04^2)$ as an additive effect to an object's apparent visual magnitude.² The intensity relative to the sun's apparent brightness generated from each facet and reflected in the direction of the observer is

¹ Data obtained from ExoAnalytics marketing video on YouTube titled, "Commercial Space Situational Awareness Solutions" at timestamp 2:53, accessed via <https://www.youtube.com/watch?v=kKQLiqM42Xw&t=3s>.

² Personal communications. Dr. Tamara Payne, Applied Optimization, Inc. July 2018.

$$S_i = (dR_{d,i} + sR_{s,i})A_i\pi(\hat{N}_i \cdot \hat{L})(\hat{N}_i \cdot \hat{V}) \quad (2)$$

where d and s are the fraction of the spectral and diffuse bidirectional reflectance values, $R_{d,i}$ and $R_{s,i}$, respectively, A_i is the facet surface area, \hat{N}_i is the surface unit normal vector, \hat{L} is the sun to RSO unit vector, and \hat{V} is the RSO to observer unit vector. Inspecting the spectral term from [10],

$$R_{s,i} = \frac{DG_iF}{\pi(\hat{N}_i \cdot \hat{L})(\hat{N}_i \cdot \hat{V})} \quad (3)$$

where D is the facet slope distribution function, G_i is the geometrical attenuation factor, and F is the surface reflectance of a perfectly smooth surface, demonstrates the dependance of reflectance on both material and geometric components. The material related elements that make up the F term, namely the diffuse and spectral reflectance coefficients for each facet, $C_{d,i}$ and $C_{s,i}$, influence the apparent brightness and how an RSO's dynamics are affected by solar radiation pressure. Spacecraft reflectance and surface area parameters implemented in the simulation are listed in Table 1. The reflected light vector and relative surface angles are depicted in Fig. 2. The 2 kHz value is chosen to ensure at least a kilohertz order of magnitude is available for acoustic analysis after application of the Nyquist Theory, to adequately capture any event frequencies, and to minimize computational requirements.

Vibration Model To simulate a thruster fire event, a fixed-free cantilever beam mode for the solar panel and a face shear mode for the satellite bus are induced as depicted in Fig. 3 and Fig. 4. A simple sinusoidal oscillation model is used for the satellite bus and solar panel surface unit normal vectors at the desired frequency to achieve the effect of a vibrating surface. It is assumed no complex deformation exists in the solar panel and thus the axis of rotation for the rigid wing model is defined at the wing-box interface. A three-dimensional surface deformation and macro model simulation should be used for an improved representation of a satellite's photometric event fingerprint. It seems reasonable that the simplistic model implemented herein and reality exhibit behavior on the same order of magnitude due to the small surface displacement magnitudes involved, especially for the satellite bus represented by the box model.

A range of burn durations less than or equal to five seconds are investigated – a realistic value for collision avoidance maneuvers. The event frequency is chosen somewhat arbitrarily to be 58 Hz but is loosely based on anecdotal and proprietary industry evidence that modes below 50 Hz are deliberately damped on various satellites due to their instrument vibration isolation requirements. It appears that some active satellite vibration modes exist in the 3–12 Hz range from on-orbit test data [11]. Another study that used cameras mounted on the GOSAT satellite to analyze solar panel vibrations caused by thermal snap and gas jet thruster firing events showed that a 0.215 Hz out-of-plane and 0.459 Hz in-plane mode were observed [12]. Both sets of on-orbit test data generally agree with the expected first natural frequency of a solar

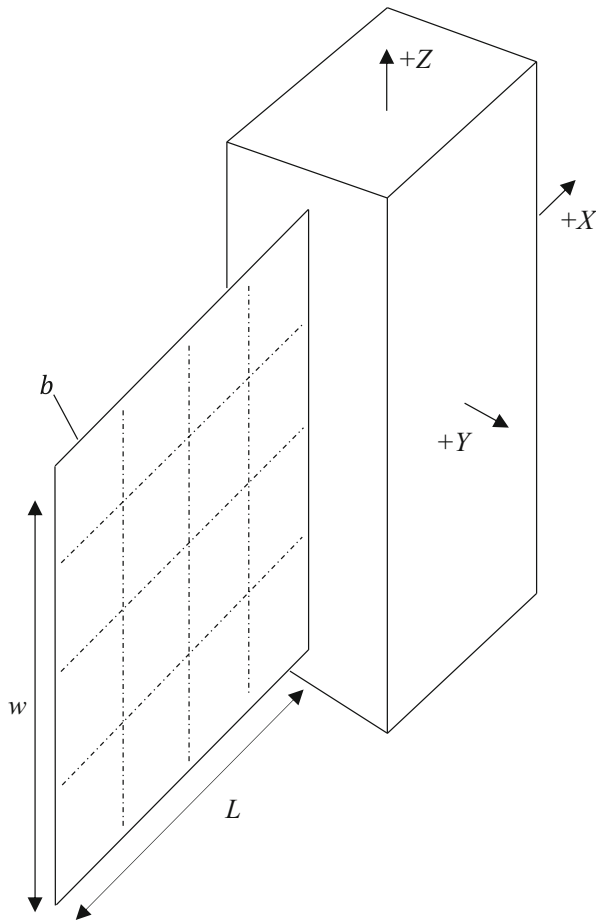


Fig. 1 Box-wing satellite model used for synthetic light curve generation, vibration model, and orbit determination

array described by the Table 2 parameters and fixed-free cantilever beam calculation in Eq. (4),

$$f_1 = \frac{K_1}{2\pi} \sqrt{\frac{EI_{yy}}{\omega L^4}} = 1.90\text{--}2.14 \text{ Hz} \quad (4)$$

Table 1 Cook-Torrance model parameters used in generating the light curve

Surface Area	Symbol	Value	Material	$C_{d,i}$	$C_{s,i}$
+X / -X Face	A_x	6 m ²	MLI Kapton	0.04	0.59
+Y / -Y Face	A_y	8 m ²	MLI Kapton	0.04	0.59
+Z / -Z Face	A_z	12 m ²	White Paint / Germanium Kapton	0.80 / 0.28	0.04 / 0.18
Solar Panel	A_{sp}	15 m ²	Solar Cells	0.04	0.04

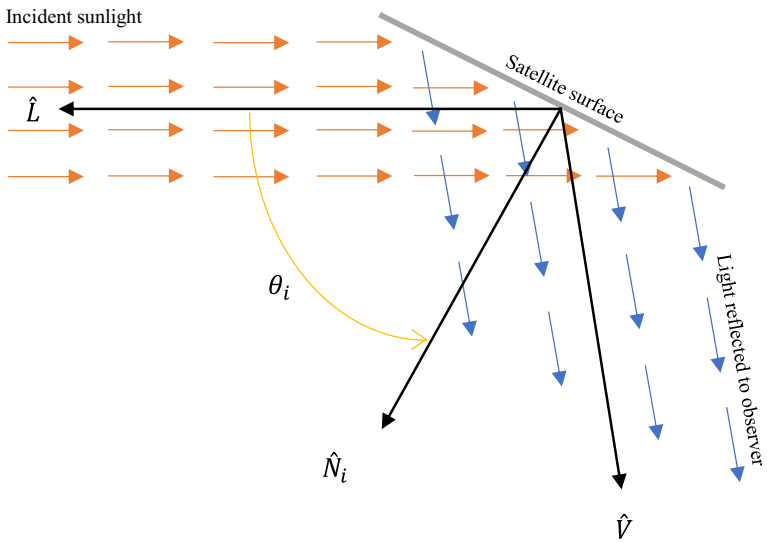


Fig. 2 Illustration of the relative surface angles defined for use in the synthetic light curve simulation

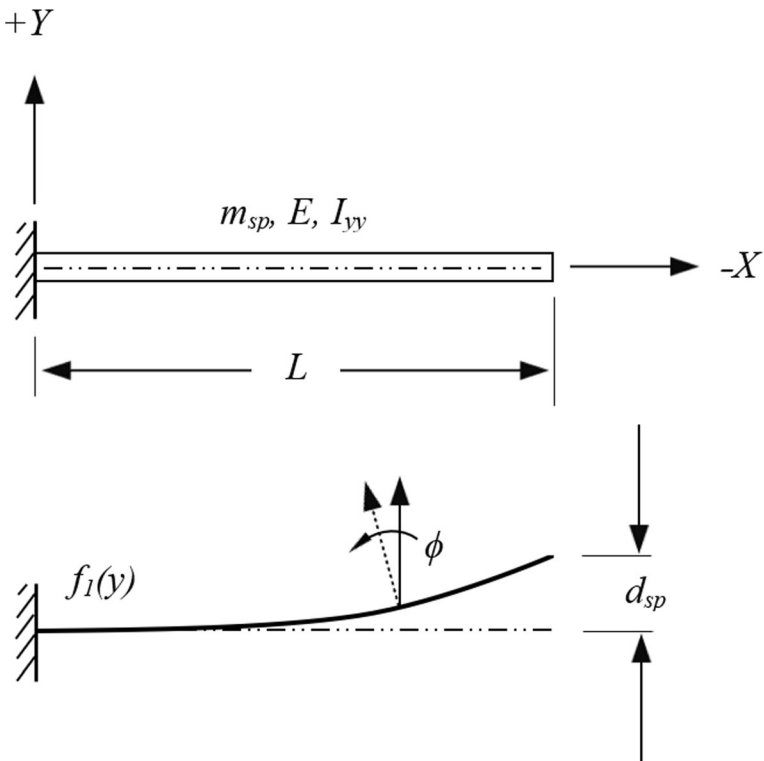


Fig. 3 (Top) Fixed-free cantilever beam approximation of the satellite solar panel and (bottom) first vibration mode shape

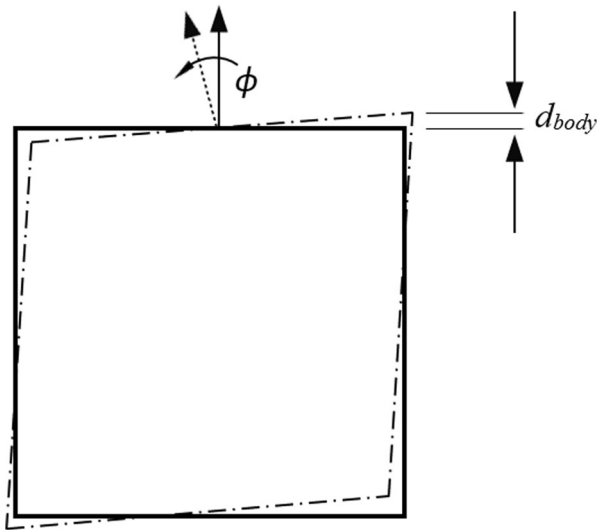


Fig. 4 Face shear vibration mode induced in the satellite body

where K_1 is the first mode parameter constant equal to 3.52 and ω is the uniform load per unit length. The solar panel is designed to mimic the specifications in [13, 14] and the material is assumed to be an aluminum composite layer with silicon solar cells. If a rectangular shaped solar array with dimensions of $6.0 \text{ m} \times 2.5 \text{ m}$ were simulated, the expected first natural frequency is calculated as 0.79 Hz.

If the lower natural frequencies are not intentionally damped, the 58 Hz value is likely overzealous if attempting to emulate a detectable event as the largest displacements will be generated from the first mode. The expected natural frequencies seem to suggest that collecting hyperteperal data in the kilohertz range is overkill. However, the high-rate collection remains useful in increasing event epoch definition precision and thus parameter estimation accuracy discussed further in Section 4, is also useful in supporting the subsystem characterization efforts from an acoustic standpoint in Section 2, and helps separate the effects of various noise sources from event frequencies reviewed in Section 6. Again, it is postulated that the acoustic interpretation of a satellite event can augment traditional frequency analysis like the Voyager 1 example

Table 2 Satellite structural parameters

Parameter	Value	Units	Symbol
Satellite bus (box) mass	1900 kg	kg	m_{sat}
Solar panel (wing) mass	100.0	kg	m_{sp}
Solar panel width	3.872	m	w
Solar panel length	3.872	m	L
Solar panel thickness	25.0	mm	b
Area moment of inertia	5042.92	mm^4	I_{yy}
Modulus of elasticity	13.3–16.8	GPa	E

to identify subsystem characteristics, e.g. a momentum wheel desaturation event would sound different than an imaging instrument scanning a target.

While the 58 Hz event frequency is referenced for the following analysis, the conclusions remain the same if it were run at a lower magnitude nearer the first natural frequency. A range of surface displacement values are simulated at the event frequency such that a minimum detectable displacement threshold can be determined. All referenced surface displacement values are calculated as the peak or largest deflection at the extrema of the box face and solar panel surface areas respectively as defined in Eq. (5), Eq. (6), and Figs. 3–4 as

$$d_{body} = \sin\phi \sqrt{\frac{A_z}{4}} \quad (5)$$

$$d_{sp} = \sin\phi \sqrt{A_{sp}} \quad (6)$$

where ϕ is the angle by which the surface unit normal vectors are rotated. The face shear mode surface unit vector rotation point for the box model is defined on its area centerlines, hence the factor of four in the denominator of Eq. (5). The box-wing interface acts as the rotation point for the fixed-free beam mode in Fig. 3. The simulation also assumes a step function for the thruster ignition and shut-off events with no thrust profile effects included.

Large Displacement Test Case To study the effects of a simulated maneuver on the apparent visual magnitude, an arbitrarily large displacement test case is run with and without the additive $N(0, 0.04^2)$ noise from the atmosphere. Results of the proof of concept are shown in Fig. 5. The simulated maneuver begins at the 1.0 s since epoch tick mark. A peak surface displacement d_{body} and d_{sp} on the order of tens of centimeters is needed to visually detect a change in apparent visual magnitude in a time series plot. A displacement value this large is unrealistic and would be a destructive mode. Potentially realistic surface displacements of the single- to sub-centimeter range are lost to the atmospheric noise as in Fig. 6 and require more advanced methods to detect an event, placing importance on the signal-to-noise ratio achieved by the optical equipment utilized for data collection discussed further in Section 6. The +11.1 m_v average apparent visual magnitude value seems reasonable for GEO distances assuming the reflectance properties defined in Table 1.

Inferring Signals from Noise Structure

To investigate if any realistic displacement magnitudes can be detected in the presence of atmospheric scintillation, three techniques were implemented. The first is a visual spectrogram review, second a Fast Fourier Transform (FFT), and third a custom cross-correlation scanning algorithm. The data collection window lasted six seconds with a simulated dynamic event occurring from 2.0–4.0 s.

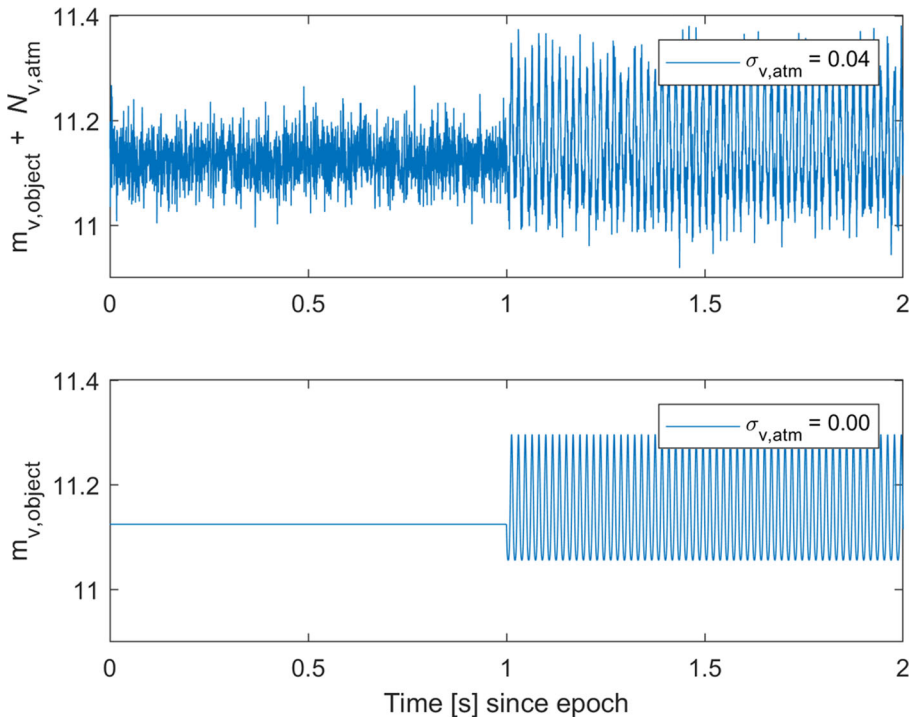


Fig. 5 Proof of concept synthetic light curve test simulation with unrealistically large d_{body} displacement of 34.41 cm and d_{sp} of 76.94 cm with (top) and without (bottom) atmospheric noise added to the event signal that begins at 1.0 s

Spectrogram Analysis Using MATLAB's *pspectrum* function to analyze a range of satellite body and solar panel displacement simulations yielded interesting characteristics including 2 N harmonics for the impractical d_{body} case of 34.41 cm in Fig. 7, likely generated by neighboring satellite body surfaces. Continually decreasing the displacement magnitude demonstrated a loss of visual spectrogram detection between 1.73–3.46 cm for d_{body} and 3.87–7.75 cm for d_{sp} as shown in Fig. 7. While the underlying technique used in the *pspectrum* function is an FFT, the function itself required a substantial amount of tuning to properly identify a signal with a visual inspection. Thus, a more direct analysis is implemented in the following subsection.

Fourier Transform A slightly different formulation of the short-time Fourier Transform in MATLAB using the *fft* function that implements a single-sided amplitude spectrum analysis was performed on the same data to determine if analyzing the raw output would allow for increased signal resolution. Unlike the spectrogram, the direct FFT power output allowed for an obvious event detection at the simulated 58 Hz event frequency as shown in Fig. 8. Decreasing the displacement magnitude d_{body} again from 1.73 cm demonstrated a loss of signal near 1.0 cm with this technique.

Cross-Correlation Scanning Algorithm The base form of both the Fourier Transform and the cross-correlation technique is a convolution and thus they both

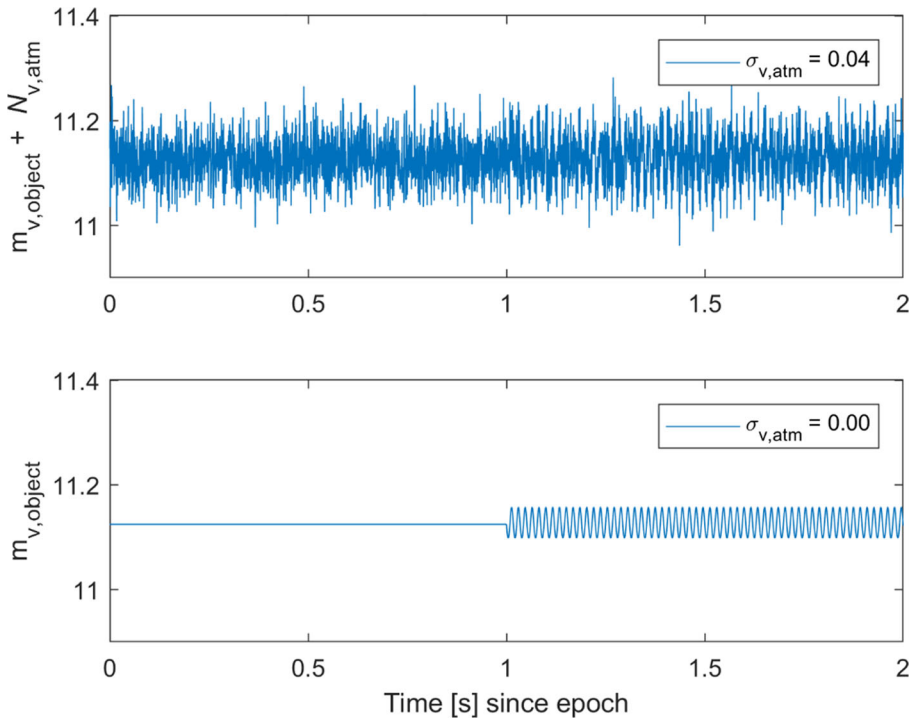


Fig. 6 Another large event signal generated from displacements with magnitudes d_{body} of 8.66 cm and d_{sp} of 19.36 cm already demonstrating visual loss of event signal (*bottom*) to the atmospheric noise corrupted signal (*top*)

operate in a similar mathematical fashion. Some of the discrete windowing parameters in the FFT algorithms employed herein warranted a look at cross-correlation to determine if any further resolution improvements could be made. Thus, a custom cross-correlation signal scanning algorithm using MATLAB's *xcorr* function was written to scan all possible frequencies, phase lag, and burn durations in an attempt to find the highest correlated reference signal [15]. The range of possible values for vibrational mode frequency parameters is plausibly constrainable to the 0–100 Hz range based on the natural frequency analysis in Section 3.1 which significantly reduced the search space. Thus, a proof of concept test case is run using the same large displacement as Fig. 7 showing successful event resolution in Fig. 9. Implementing the scanning algorithm on prior loss of signal cases slightly improved the d_{body} detection criteria to 7.0 mm as shown in Fig. 10. A best-case atmospheric noise distribution of $N(0, 0.03^2)$ allowed detection to a 5.2 mm displacement for the satellite body and 1.16 cm for the solar panel with this technique.

The signal-to-noise ratio (SNR) for all simulations was calculated using Eq. (7) in units of decibels and yielded the values in Table 3. The numerator inside the log term of Eq. (7) is the variance of the event signal while the denominator is that of the atmospheric noise source, 0.04^2 in most cases. The results suggest a lower bound on the effective SNR near -27.55 dB for satellite event detection via cross-correlation.

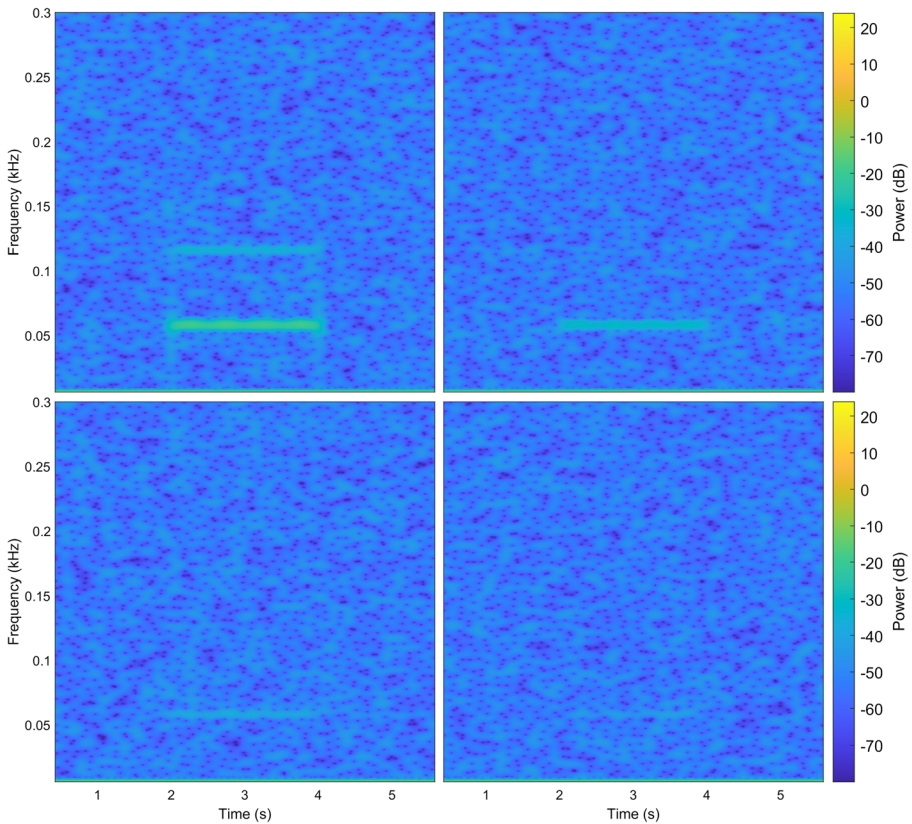


Fig. 7 Spectrogram results using the largest four solar panel and satellite body displacements from Table 3 demonstrating the 58 Hz dynamic event detection with 2 N harmonics present at -16.67 dB (*top left*) decreasing signal strength near -27.10 dB (*top right*) lowest plausible event detection at -36.91 dB (*bottom left*) and finally loss of visual event detection (*bottom right*)

$$SNR = 10 \log_{10} \frac{\sigma_{v,sig}^2}{\sigma_{v,atm}^2} \quad (7)$$

While this simulation assumed the atmosphere was the dominant source of apparent visual magnitude uncertainty, other sources such as instrumentation error should be considered and carefully calibrated. This research also assumes maneuvers are observable at night and the start and end epochs of the propulsive event are directly observable with a high rate, sensitive photometer. It may be possible to extend this technique into the non-visible spectrum to detect events during the daytime. Additionally, the target RSO must be acquired and tracked within the telescope field of view (FOV) throughout the event duration. For satellites in LEO this could pose a challenge, especially for long, non-impulsive maneuvers. It seems plausible to employ these tactics to satellites in GEO based on their more stationary target orbits. The logical next inquiry that arises is what the limiting detection factor becomes if there were no atmospheric turbulence to corrupt an event signal. An immediate application for such a scenario with no or less atmosphere is a satellite-to-satellite observation at a geosynchronous orbital distance. Other noise sources such as vibration induced by fuel slosh or other spacecraft subsystem operations may need to be overcome once the atmosphere error is eliminated.

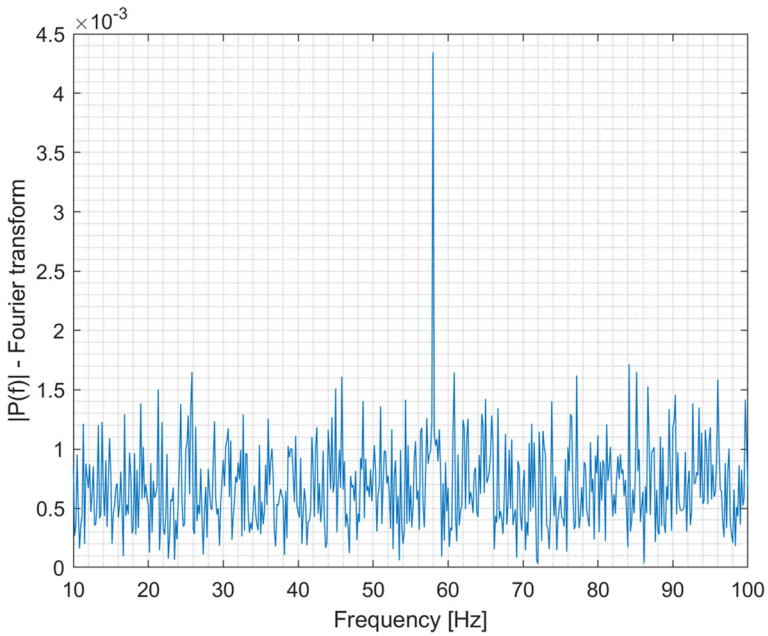


Fig. 8 Fast Fourier Transform demonstrating a 58 Hz dynamic event detection for the 1.73 cm d_{body} and 3.87 cm d_{sp} satellite and solar panel displacement simulations in units of light intensity squared per Hz

Considering the absolute best-case atmospheric scintillation assumptions and achieved SNR from simulation, a detectable d_{body} value of 5.20 mm may be approaching the realm of

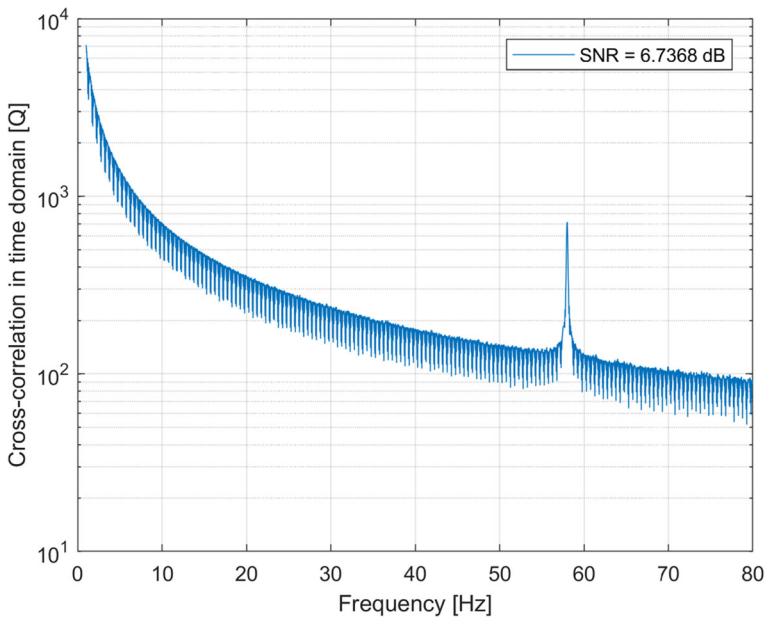


Fig. 9 Proof of concept cross-correlation scanning algorithm test simulation with the unrealistically large surface displacements of 34.41 cm and 76.94 cm for d_{body} and d_{sp} demonstrating event detection at 58 Hz

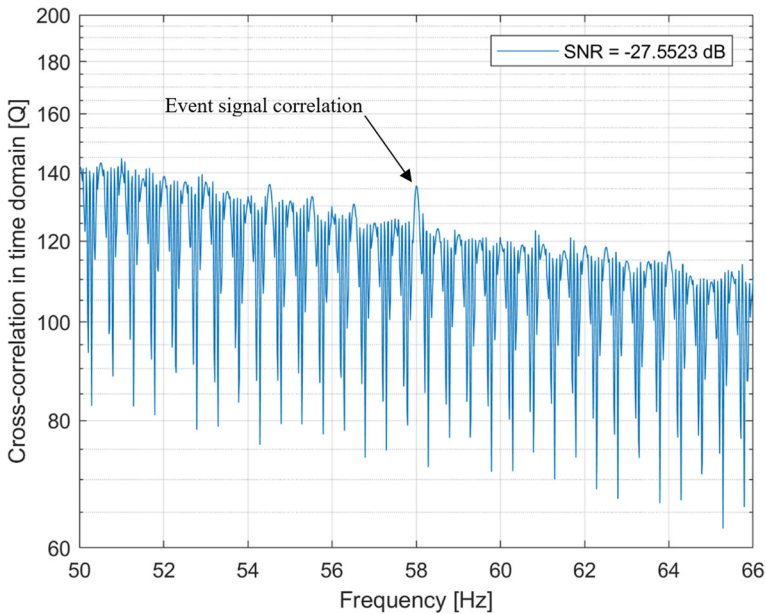


Fig. 10 Cross-correlation results for the 6.93 mm d_{body} and 1.55 cm d_{sp} simulations demonstrating dynamic event detection at 58 Hz

a realistic satellite bus displacement although it still has the potential to remain a destructive mode at this order of magnitude. With regard to the best-case solar panel displacement demonstrating a detection, considering the tip deflection of 1.16 cm at the end of a 3.872 m fixed-free cantilever beam seems like a plausible magnitude for an on-orbit mode. However, more research using a three-dimensional macro vibration model with precise material and shape selections would be required to determine realistic on-orbit displacement values given an accurate forcing function from a propulsive event.

Maneuver Estimation

Using the dynamic event detection techniques of the prior section, photoacoustic sensing provides a means to directly timestamp maneuvers and other operational events

Table 3 Signal-to-noise ratio values corresponding to displacement magnitudes

d_{body}	d_{sp}	$\sigma_{v, atm}$	SNR
5.20 mm	1.16 cm	0.03	-27.55 dB
6.93 mm	1.55 cm	0.04	-27.55 dB
1.73 cm	3.87 cm	0.04	-19.59 dB
3.46 cm	7.75 cm	0.04	-13.57 dB
8.66 cm	19.36 cm	0.04	-5.59 dB
34.41 cm	76.94 cm	0.04	+6.74 dB

in space. With event epoch error bounds as large as a full orbital period demonstrated in some of the prior literature review, it becomes impossible to accurately estimate spacecraft parameters that involve any sort of time dependency with this technique. However, direct event observations via hypertemporal photometry provide the ability to estimate impulse-related spacecraft parameters that were not possible with legacy techniques due to the large error incurred by generally comparing orbital changes before and after an estimated event epoch. While tracking the RSO throughout the entire event duration would support photoacoustic characterization efforts, only the initial and final event epochs require observability to allow for estimation of the following parameters.

For propulsive events, the ability to directly define the impulse duration allows for estimation of Δv magnitude, direction, and maneuver type once the RSO state is resolved to a desired level of uncertainty post maneuver. We define “near real time” estimation as the time duration between maneuver end and post-maneuver state resolution. To study how sensitive the aforementioned parameters are to direct event start and end epoch observation precision assumed via photoacoustic sensing, a Δv simulation is run. Satellite operators at Optus, an Australian telecommunications company, were kind enough to provide both the states before and after station-keeping maneuvers as well as exact maneuver start epochs and burn durations for various satellites in their constellation in GEO as a comparison to truth.

The dynamic model used for the propagation of the Optus satellite included a 20×20 EGM-96 gravity model, luni-solar perturbations, and an area-averaged exponential drag and solar radiation pressure model. It is assumed that the ballistic coefficient and equivalent solar coefficient-area-mass ratio were estimated via observations made on the RSO prior to observing a maneuver. Propagating the true Optus states provided before and after the maneuver to the given maneuver end epoch and computing their differences yielded the results in Table 4. Using a ± 0.50 s uncertainty on the maneuver end epoch incurred the errors also listed in Table 4. Thus, for photoacoustic sensing to act as a reliable parameter estimation scheme, event start and end epoch observations must perform to a tenth-second or less uncertainty range to bound the estimation error to low single digit percentages. In the ExoAnalytics data referenced in Section 3, it is easy to determine the thruster plume event epoch to less than 0.20 s of error when utilizing an apparent eight hertz collection rate, giving confidence to the notion that hypertemporal methods would allow for even more precise temporal event definition.

Table 4 Delta- v estimation results in terms of percent error of reference values

Parameter	Accuracy
Δv magnitude (exact epochs)	$\leq 0.52\%$ of true value
Δv (+0.5 s epoch)	$\leq 7.85\%$ of true value
Δv (0.5 s epoch)	$\leq 59.8\%$ of true value
Δv direction	≤ 1.72 degrees of true pointing vector
Maneuver type	Correct id. of N-S station-keeping
Maneuver duration	No obs. Data to support comparison yet

To demonstrate how RSO state uncertainty contributes to Δv parameter estimation error, a simple time calculation using standard orbital velocities and a range of covariance sizes is computed. For example, if the RSO state can be resolved to a 100-m 3σ state uncertainty at the maneuver end epoch in the along-track direction, the additive effect on the Table 4 event epoch uncertainty parameters can be bounded near 35 ms for GEO and 15 ms for LEO. This result suggests the limiting factor in near real-time Δv parameter estimation accuracy will be the observational event detection epoch precision.

Orbit Determination The prior Δv simulation assumed operator provided states were available post-maneuver – an unrealistic assumption when studying uncooperative or non-operational RSOs. To investigate how quickly a post-maneuver RSO state can be resolved via observation, an Extended Kalman Filter (EKF) is implemented using simulated range and range-rate measurements from three near-equatorial stations for an RSO in a 791 km near-circular orbit. A State Noise Compensation (SNC) algorithm was included in the EKF to prevent filter saturation and account for any dynamic model uncertainty. The ground station locations were chosen to mimic the Kwajalein Atoll, Diego Garcia, and Arecibo sites currently in the U.S. Space Surveillance Network, although the Arecibo site was not visible during the time span shown in Figs. 11–12. A complex Earth model using an FK5 precession, nutation, and polar motion correction and the effects of light time were accounted for in the measurement simulation. Measurement uncertainties based on demonstrated values by LeoLabs [16, 17], observation frequency, and a priori covariance values are given in Table 5. To inject

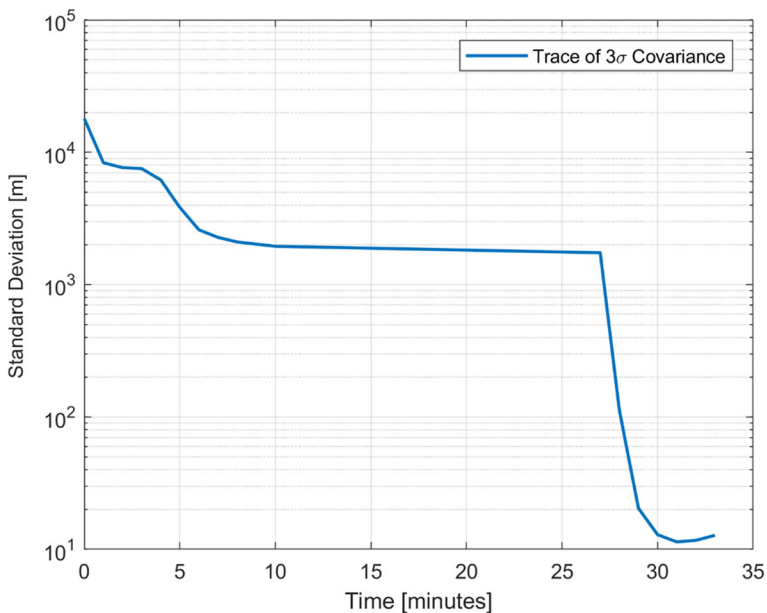


Fig. 11 Post-fit state 3σ standard deviation trace output from the EKF starting from maneuver end epoch to solution convergence. The apparent discontinuity at 27 min is caused by obtaining measurements from the Kwajalein Atoll station acquired after a measurement gap from 10 to 27 min – the new measurement geometry reduces uncertainty

operational realism into the scenario, a seventeen-minute observation gap is included in the time study between the two visible ground stations. As seen in Figs. 11–12, the EKF required eleven observations at a sixty second interval over a span of thirty minutes to achieve a 13-m 3σ state uncertainty post maneuver. Back propagation to the maneuver end epoch with a Rausch-Tung-Striebel smoother maintained an uncertainty well within the referenced 100-m 3σ state uncertainty bound referenced previously.

With more consistent measurements, priority tasking, and ideal station coverage, the uncertainty convergence time can be improved. While the 3σ state uncertainty is a common metric used to confidently resolve an RSO state, it is not the only way to allow near real time estimation. For the same simulation, the measurement residuals and innovations covariance in Fig. 12 can give clues to solution stability. After only two measurements, the range residual has stabilized and the 3σ innovations covariance has achieved a steady 20-m value. Thus, it seems generally plausible to estimate Tables 4 and 6 parameters within five minutes of an active satellite maneuver using this technique and given assumptions. Studying residual behavior to indicate state stability should be used with caution as residuals alone do not guarantee an accurate orbit and should be later substantiated with the traditional state covariance convergence or other metrics.

Spacecraft Operational Assessment

Near real time Δv and maneuver type estimation defined in Section 4 allow for rapid response to uncooperative satellite operations and anomalous unmodeled dynamic events. Knowledge of these parameters combined with the now directly observed event

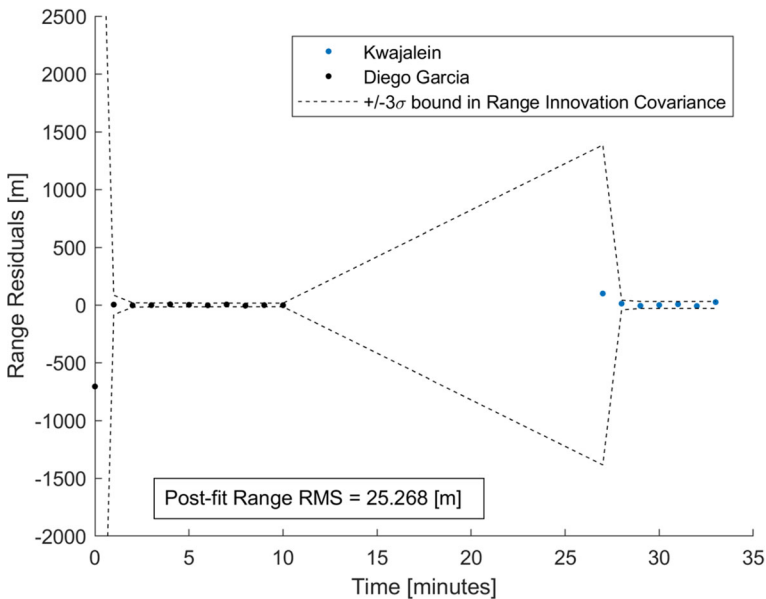


Fig. 12 RSO range residuals and innovations covariance indicating a stable EKF solution after only 1–2 observations

Table 5 Orbit determination a priori uncertainty assumptions

Parameter	Value
Range uncertainty (σ)	15.0 m
Range-rate uncertainty (σ)	10.0 cm/s
A priori position offset	1.0 km
Observation frequency	60.0 s
A priori position covariance	4.0 km ² /s ² per position diagonal
A priori velocity covariance	1.0 m ² /s ² per velocity diagonal

epochs thanks to the photometric event detection techniques of Section 3 allow for a deeper understanding of spacecraft operational parameters specific to propulsive events. Through the application of orbital momentum and energy conservation equations about the known maneuver impulse, the prior techniques can be extended to estimate thruster mass flow rate, specific impulse, and fuel consumed given an a priori mass estimate. While the origins of the specific orbital momentum and energy integrals of motion in Eq. (8) and Eq. (9) are well established, it is important to understand their derivation and application as it has direct implications into the ability to estimate certain spacecraft mass properties. The base form of the specific orbital momentum \hat{h} is defined as

$$\hat{r} \times \hat{v} = \hat{h} \quad (8)$$

where \hat{r} is the satellite position vector, \hat{v} is its velocity vector, and the specific orbital energy ε is defined by

$$\frac{v^2}{2} - \frac{\mu}{r} = \varepsilon \quad (9)$$

where v and r are the magnitudes of the state vectors from Eq. (8) and μ is Earth's gravitational constant. To infer operational information about an active satellite, the maneuver specific parameters must be related to known orbital quantities. In its most basic form, a maneuver is simply an impulse on this system and the initial and final orbital momentum and energy are calculable quantities from the research of Section 4.

Table 6 Estimation results for the Optus spacecraft operational parameters, in terms of percent error to maintain proprietary nature of propulsion system values

Parameter	Accuracy
Mass flow rate	$\leq 2.0\%$ of true value
Specific impulse	$\leq 3.0\%$ of true value
Fuel consumed	$\leq 1.0\%$ of true value
Exhaust velocity	Agrees with thruster class values

Thus, it is plausible to expand the specific orbital momentum and energy equations to their mechanical forms and include the varying work and impulse terms imparted by any dynamic events. The general form of the conservation of momentum equation is defined in Eq. (10) as

$$\int_{t_i}^{t_f} F dt = m_f v_f - m_i v_i = \Delta p \tag{10}$$

where F is the force imparted on an object from time t_i to t_f , Δp is the total change in momentum, and m_i , m_f and v_i , v_f are the initial and final masses and scalar velocities of the object, respectively. The work W imparted on an object due to a force F is defined in Eq. (11) as

$$W = \int_C F \cdot dx = \int_{x(t_i)}^{x(t_f)} F \cdot v dt = E_f - E_i \tag{11}$$

where C is the trajectory from initial position $x(t_i)$ to final position $x(t_f)$, v is the velocity, and E_i , E_f are the initial and final energies. Extending these basic equations to the orbit problem and converting from scalar to vector quantities while including any rotational terms will yield the expanded forms in Eq. (12) and Eq. (13). These forms assume the only force contributing to the respective work and impulse integrals is due to the maneuver and that the object mass, position, and velocity are time varying. For the full orbital impulse-momentum conservation equation,

$$\begin{aligned} m_i \hat{r}_i \times \hat{v}_i + \int_{t_i}^{t_f} \hat{r}(t) \times (m_i - \dot{m}t) \hat{a}_{th}(t) dt + \int_{t_i}^{t_f} \hat{\tau}(t) dt + I_i \hat{\omega}_i + h_i \\ = (m_i - \dot{m}\Delta t) \hat{r}_f \times \hat{v}_f + I_f \hat{\omega}_f + h_f \end{aligned} \tag{12}$$

where the parameter $\hat{a}_{th}(t)$ denotes the time-varying acceleration vector due to thrust, \dot{m} is the thruster mass flow rate, $\hat{\tau}(t)$ is the time-varying rotational torque imparted on the spacecraft by the maneuver, Δt is the duration of the impulse, I_i and I_f are the initial and final mass moments of inertia, $\hat{\omega}_i$ and $\hat{\omega}_f$ are the initial and final angular velocity, and finally h_i and h_f are the initial and final momentum wheel terms. Regarding the orbital work-energy conservation equation,

$$\begin{aligned} m_i \left[\frac{1}{2} \hat{v}_i^2 - U_E(\hat{r}_i) \right] + \frac{1}{2} \hat{\omega}_i^T [I_i] \hat{\omega}_i + \int_{t_i}^{t_f} \left[(m_i - \dot{m}t) \hat{a}_{th}(t) \right] \cdot \hat{v}(t) dt + \\ \int_{t_i}^{t_f} \hat{L}(t) \cdot \hat{\omega}(t) dt = (m_i - \dot{m}\Delta t) \left[\frac{1}{2} \hat{v}_f^2 - U_E(\hat{r}_f) \right] + \frac{1}{2} \hat{\omega}_f^T [I_f] \hat{\omega}_f \end{aligned} \tag{13}$$

where the U_E terms describe the gravitational potential energy at a given position and $\hat{L}(t)$ is the angular work performed over the maneuver.

Momentum or energy losses due to imperfect thrust vectoring, momentum wheel saturation, or the change in moment of inertia due to decreasing spacecraft mass are assumed to be negligible for a satellite with a nadir aligned, velocity constrained attitude profile over a short maneuver duration. Thus, the rotational energy, work, torque, and momentum terms cancel over the time span of the maneuver and can be removed from the equations. The remaining form consists of two equations and five unknowns – mass, mass flow rate, and the position, velocity, and acceleration due to thrust as functions of time during the impulse. To solve for the time varying functions, one can divide the Δv magnitude by the burn duration to get the average acceleration magnitude over the maneuver. The direction of the acceleration is the same as the Δv pointing vector. Thus, the force model can be augmented to include the acceleration due to the thrust and the satellite position and velocity as functions of time can be discretized. A fourth order polynomial is then used to fit each component of the discretized state over the maneuver, thus reducing the unknowns from five to two.

An analytical form of the acceleration due to thrust as a function of time can also be formulated based on the specific impulse in Eq. (14) and rocket equations defined in Eq. (15) as

$$F_{th} = I_{sp}g_0\dot{m} = v_e\dot{m} = ma_{th} \tag{14}$$

where F_{th} is the overall force imparted on the satellite due to thrust, I_{sp} is the specific impulse of the thruster, g_0 is the standard acceleration due to gravity at sea level, a_{th} is the acceleration due to thrust, and v_e is the exhaust velocity. Continuing with the rocket equation,

$$\frac{\Delta m}{m_i} = 1 - e^{-\frac{\Delta v}{I_{sp}g_0}} \tag{15}$$

where Δm is the change in mass and Δv is the change in velocity imparted on the satellite, or simply the delta-v. Solving for the scalar acceleration due to thrust, vectorizing, and injecting time dependency yields the form in Eq. (16). The acceleration unit vector as a function of time $\hat{a}_u(t)$ can either use the polynomial form mentioned previously or the constant Δv relative pointing vector derived in Section 4.

$$\hat{a}_{th}(t) = \frac{-\Delta v \dot{m}}{(m_i - \dot{m}t) \ln \left[\frac{1 - \dot{m}\Delta t}{m_i} \right]} \hat{a}_u(t) \tag{16}$$

Substitution into the simplified mechanical momentum and energy equations yields their final forms in Eq. (17–19) below.

$$m_i \varepsilon_i + \int_{t_i}^{t_f} \left[\frac{-\Delta v \dot{m}}{\ln \left[\frac{1 - \dot{m}\Delta t}{m_i} \right]} \hat{a}_u(t) \right] \cdot \hat{v}(t) dt = (m_i - \dot{m}\Delta t) \varepsilon_f \tag{17}$$

$$\varepsilon_k = \begin{cases} \frac{1}{2} \widehat{v}_i^2 - U_E(\widehat{r}_i) & \text{for } k = i \\ \frac{1}{2} \widehat{v}_f^2 - U_E(\widehat{r}_f) & \text{for } k = f \end{cases} \quad (18)$$

$$m_i \widehat{r}_i \times \widehat{v}_i + \int_{t_i}^{t_f} \widehat{r}(t) \times \left[\frac{-\Delta v \dot{m}}{\ln \left[\frac{1 - \dot{m} \Delta t}{m_i} \right]} \widehat{a}_u(t) \right] dt = (m_i - \dot{m} \Delta t) \widehat{r}_f \times \widehat{v}_f \quad (19)$$

With only mass and mass flow rate as the remaining two unknown parameters and having two equations, it seems as if it would be possible to solve the system of equations. However, the prior conversion from specific to mechanical energy and momentum in Eq. (12) and Eq. (13) sheds the linear independence with respect to the mass and mass flow rate terms. If one attempts to solve for the two unknown parameters, the resulting output will show no unique solution. One potential workaround for the linear dependence problem is to determine if there are any numerical mass and mass flow rate pairs that satisfy Eq. (17–19). Unfortunately, inputting a grid of mass parameter pairs in a Monte Carlo fashion produces another ambiguous solution space with a range of pairs that satisfy the system balance. Thus, application of momentum and energy to the orbital impulse problem does not allow for standalone estimation of mass and mass-flow rate and an a priori estimate of one or the other is necessary to solve either equation.

Utilizing the true spacecraft mass provided by Optus in the same simulation from Section 4 to solve for the mass flow rate included in Eq. (17) yields an estimate within 2 % of the true value. Use of Eq. (14) and Eq. (15) then allows for calculation of the thruster specific impulse and exhaust velocity with results tabulated in Table 6.

The results in this section reiterate the importance of efforts in the Space Situational Awareness (SSA) community to estimate RSO mass and the resulting operational assessments that can be gained through estimates of the Table 4 and Table 6 parameters. One mass estimation method that seems promising uses astrometric and photometric data fusion [18]. Utilizing this method to get a good a priori mass estimate would subvert the linear dependence problem discussed previously.

A potential impact of estimating fuel consumption over time is the ability to monitor if an uncooperative satellite is saving enough fuel for a proper post-mission disposal or graveyard orbit. An estimate of specific impulse also helps characterize the operational capability and mission of an active satellite. Assuming the Table 6 parameters are known in addition to the operational frequency and potentially a derived thrust profile, it is conceivable to compare these propulsion system values to known model specifications and thus constrain a specific class or even unique model to an observed event. Identifying a thruster model may help with other RSO identification parameters such as launch date or country of origin.

Observations

The experimental goal of this research was to observe an active satellite thruster fire event and apply the estimation techniques of prior sections. Satellite operators at Optus and Iridium provided their maneuver schedule such that a precise orbital location and epoch were known for each station-keeping maneuver. The optical telescopes used are courtesy of the SERC 0.7 and 1.8-m geotrackers at the Mt. Stromlo Observatory in Australia with collaboration from EOS Space Systems. The hypertemporal sampling rate detector is based on a Hamamatsu PMT sensor (H11901–20) that is sensitive over the entire visible spectrum. The photometric data is sampled at a rate of 50 kHz (up to 100 kHz), time stamped in UTC via GPS signal, and stored in binary files. The detector is built on the Beaglebone Black PC board with the real time operation software written in C++. The H11901 type PMTs operate with a highly sensitive photocathode that makes them suitable for even the most demanding photon counting applications. During the GEO observations at the 1.8 m telescope, the PMT detector was operated at the maximum gain of 4.0×10^6 and our estimations suggested that the system should respond to the low intensity of the photon flux reflected off the GEO targets.

The high sampling rate of 50 kHz is useful in that it helps separate out noise sources from any event signals. As predicted in Section 3.1, any detected events will likely manifest in the sub-100 Hz range. The effect of atmospheric scintillation is unstable and changes from 10 Hz to 100 Hz which is near the predicted event spectra. The 50 kHz sampling rate should be able to easily separate any dynamic event signatures from atmospheric effects or other noise sources. A potential limiting factor in the collection efforts is likely to be the SNR achieved by each telescope. The sensitivity of the 0.7-m telescope was defined to approximately a +9 stellar magnitude with an FOV of 0.5 deg. No sensitivity test was available for the 1.8 m due to required mirror maintenance.

Thus far, observations on these constellations have not yielded a maneuver detection yet. However, at least one anomalous event is included for further analysis. In addition to collaboration with Optus and Iridium, over twenty hours of data on 29 unique active satellites including the GLONASS constellation, Ajisai, Cosmos 2527, and Sentinel 1a & 1b were collected without any knowledge of their operational schedules. While some of the phenomena included in this section do not require hypertemporal photometric data nor photoacoustic conversion to be observed, the data are still included as a capability demonstration. Secondary measurements from LeoLabs also helped determine whether unexplained signals could be correlated to any unmodeled dynamic events.

Iridium flare Data collected on Iridium 14 revealed a classic flare, or abrupt peak in visual magnitude, due to favorable observation geometry and the relative attitude progression throughout its orbit. The flare included two auxiliary peaks on either side of the main peak shown in Fig. 13. It is likely the auxiliary peaks were caused by door-sized antennas offset by forty degrees from the panel antenna that is known to cause the main flare in light intensity. The photoacoustic playback of the flare allows for detection of the main intensity rise and fall as well as the auxiliary peaks. As this is a common

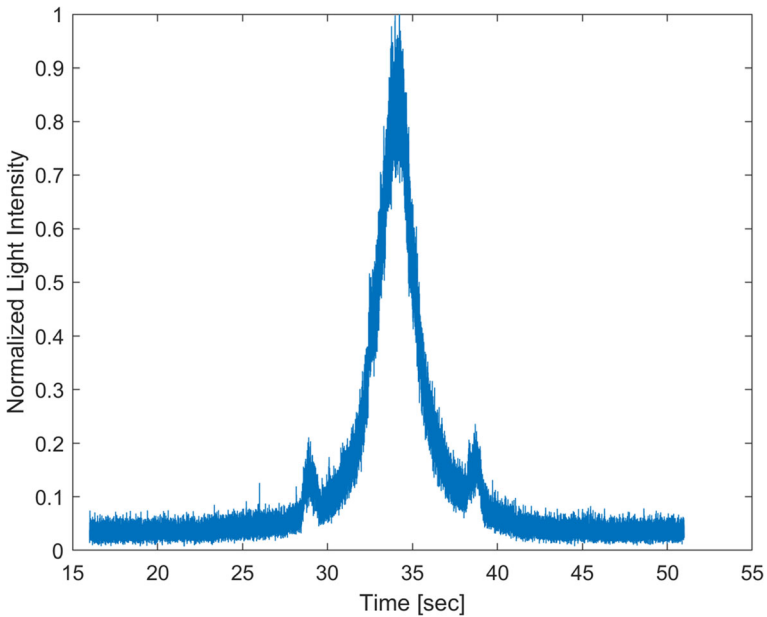


Fig. 13 Plot of normalized light intensity for an Iridium 14 flare demonstrating two auxiliary peaks, likely due to the 40 deg offset door panel antennas

satellite event that is easily detected in the photometric domain, the audio playback does not reveal any unique insights besides it being a demonstration of the acoustic domain conversion.

Ajisai tumble chirp The Experimental Geodetic Payload (EGP) satellite *Ajisai* was a useful calibration object for the detection system. *Ajisai* has a known spin rate of 1.25 Hz which can be seen in Fig. 14 plotted with the FFTW tool [19]. The photoacoustic playback of *Ajisai*'s signal can be described as a partially muted tumble chirp at the aforementioned rate, or three times the base frequency. Like the flare, deriving spin rates from photometry is a relatively

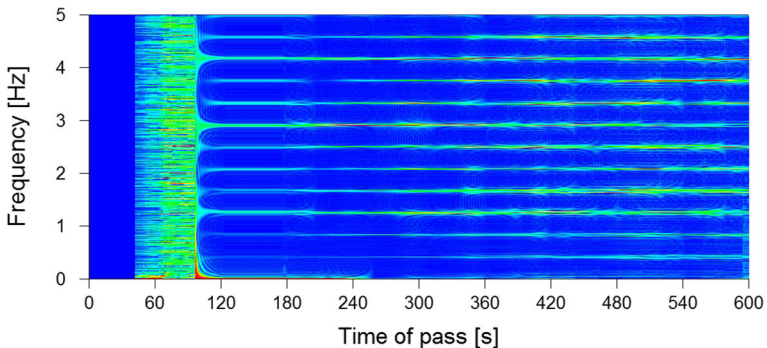


Fig. 14 Frequency spectrum of an *Ajisai* pass generated by the FFTW tool. The parallel lines originating near RSO acquisition at 100 s indicate the harmonics of the known satellite spin frequency of 1.25 Hz. Color scale is the signal power normalized to the local maximum (red) and minimum (blue) of the moving time slot of 60 s

well-known phenomenon and thus the acoustic analysis acts more as a confirmation of known RSO behavior.

SLR ticking In many of the collected data arcs, a 10 Hz and sometimes a 60 Hz signal would show up briefly and then disappear with no apparent correlation to satellite events. The signal itself sounded like a reverberating tick that was easily identifiable whenever it appeared. Eventually, it was discovered that the nearby satellite laser ranging (SLR) equipment operation correlated with the signal epochs. While the SLR operated at 60 Hz, the photometric system became blind during the laser pulses approximately every 100 ms due to what is likely a time domain aliasing effect. Thus, the 10 Hz signal can be acquired in an FFT. One example of the 60 Hz signal detection is shown in Fig. 15.

Australian power grid Another mystery signal is explained by the Australian power grid operating at 50 Hz. A commonly observed phenomenon is the flickering of exterior lights in close proximity to the observatory at two times the grid frequency as shown in Fig. 16. The lights are motion sensor activated, likely initiated by some nearby kangaroos, and thus can show up sporadically in the data. This particular signal was indistinguishable from background noise in the acoustic domain.

Uncorrelated burst-like transient A yet unexplained signal that appeared similarly at least twice across two unique satellite collections can be acoustically described as a short burst-like transient. Each time the profile appeared in the time-series data there were two distinguishable peaks. There were many other cases where a star passed the FOV which caused a gradual rise and fall in light intensity. This transient appeared much too short to be explained by a star passing. Acoustic playback of the potential event sounds somewhat noisy but does have a detectable dual-burst or knocking characteristic to it. The frequency content is rich in the sub-10 Hz range as shown in Fig. 17. It was confirmed

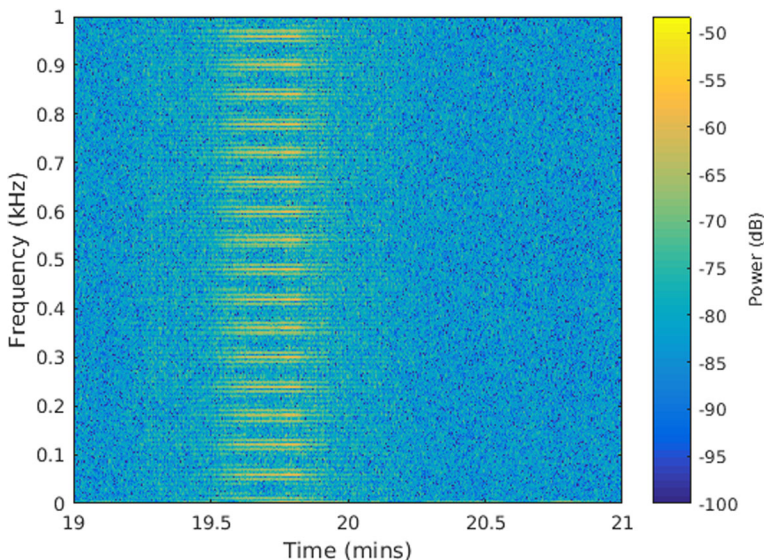


Fig. 15 Spectrogram demonstrating the 60 Hz laser pulse fundamental frequency near -57.22 dB and harmonics detected when the SLR crossed the geotracker FOV

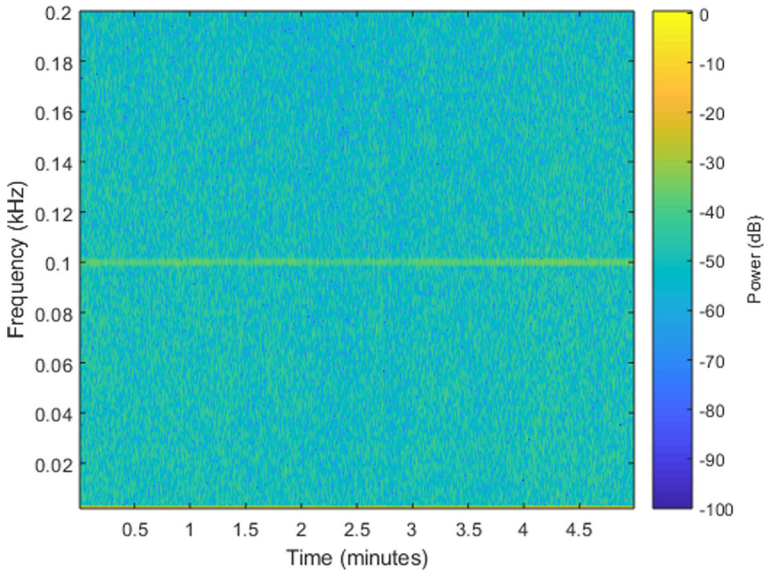


Fig. 16 Data collection attempt that captured the Australian power grid lights flickering at two times the 50 Hz grid frequency at -35.95 dB

by Iridium that no maneuvers were planned while these transients were observed. Further analysis is needed to determine if the events originated from the spacecraft or if a measurement system aberration may have been the source.

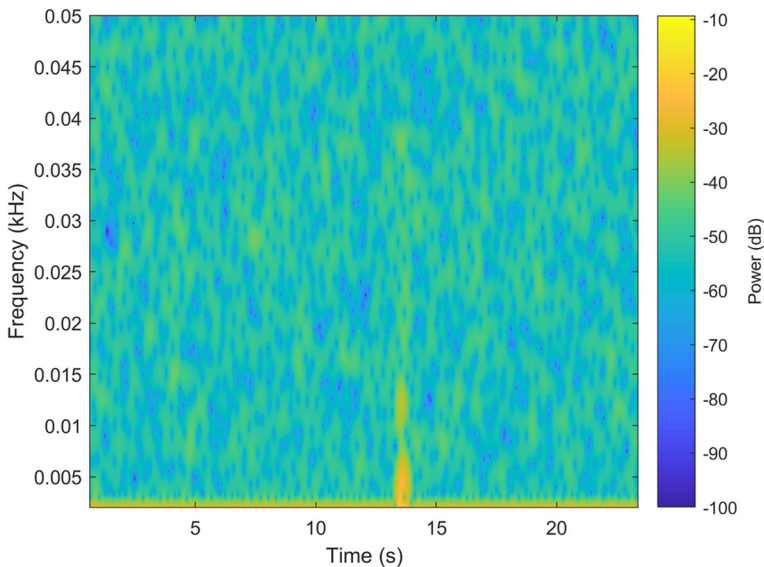


Fig. 17 Uncorrelated Iridium 14 burst-like transient displaying rich frequency content below 10 Hz at -22.55 dB

Many factors may have contributed to the experimental null finding. The propulsion system on the observed Optus satellites may have simply not induced enough vibration in the satellite body or any modes that were activated were damped. The effective SNR from the optical system also may have been insufficient to distinguish any signals from atmospheric or other noise sources. The 1.8 m telescope was unavailable for most of the collection efforts and the 0.7 m geotracker was only sensitive to $+9 m_v$ and thus the 1.8 m was likely required to detect dynamic events near the predicted $+11.1 m_v$. Also, the atmospheric condition, high clouds, water vapor, or dust could have attenuated any event signal and thus the overall intensity of light focused on the sensor may not have exceeded the noise level.

Conclusions

The research herein proposed a new method to support characterization of resident space objects by exploiting remote photoacoustic signatures. It was postulated that interpreting hypertemporal photometric data as a photoacoustic signal can support characterization of active satellites and distinguish between spacecraft subsystem events. With a maneuver start and end epoch actively observed via hypertemporal photometric data collection, it was shown that the burn duration, event frequency, Δv magnitude, direction, and maneuver type could be accurately estimated within five minutes of a completed maneuver. This near real time estimation scheme supports operational risk reduction by significantly shrinking the maneuver detection lag. It was also shown that with an a priori estimate of spacecraft mass, the thruster mass flow rate, specific impulse, exhaust velocity, and fuel consumed by a maneuver could be accurately estimated via impulse-momentum and work-energy methods. These parameters help characterize the operational capability of active satellites and can also support RSO identification. The ability to estimate fuel consumption supports efforts to monitor uncooperative satellite behavior for adherence to proper post-mission disposal actions. This research provides further motivation to experimentally detect an active satellite maneuver event via direct plume observation or vibration analysis. Current modeling suggests that relatively large, potentially destructive modal displacements are required for optical sensor detection and thus further refinements in vibration modeling and SNR improvements should be explored. The resulting knowledge that can be attained from such an event detection shows promise in characterizing RSO behavior and maintaining a sustainable space environment.

Acknowledgements The authors would like to thank Dan Slater and Rex Ridenoure for the initial seed idea that pointed us towards the light to sound conversion paradigm. Also, a bravo and thank you is deserved of our colleagues at SERC and EOS Space Systems, specifically James Bennett, James Webb, and Daniel Kucharski, for the telescope operation, data collection, and use of the hypertemporal photometric detection system. The authors would also like to acknowledge the collaborative efforts of Andrew Edwards, Tim Lilley, and Anthony Belo of Optus. Also, the collaborative sharing efforts of the Iridium operators were much appreciated. We would also like to thank Tamara Payne for valuable

discussions regarding synthetic light curve simulations and Jayant Sirohi for insight on potential box-wing vibration modes. Yet another thank you is directed to Preston Wilson for valuable discussions on acoustics. We would also like to thank LeoLabs for their maneuver detection support and helpful supplementary data analysis. Finally, we would like to thank Vishnuu Mallik for helpful references on light curve, range, and range-rate measurement simulations.

Open Access This article is licensed under a Creative Commons Attribution 4.0 International License, which permits use, sharing, adaptation, distribution and reproduction in any medium or format, as long as you give appropriate credit to the original author(s) and the source, provide a link to the Creative Commons licence, and indicate if changes were made. The images or other third party material in this article are included in the article's Creative Commons licence, unless indicated otherwise in a credit line to the material. If material is not included in the article's Creative Commons licence and your intended use is not permitted by statutory regulation or exceeds the permitted use, you will need to obtain permission directly from the copyright holder. To view a copy of this licence, visit <http://creativecommons.org/licenses/by/4.0/>.

References

1. Inter-Agency Space Debris Coordinate Committee: IADC Space Debris Mitigation Guidelines, Revision 1. United Nations Office of Outer Space Affairs, https://www.unoosa.org/documents/pdf/spacelaw/sd/IADC-2002-01-IADC_Space_Debris-Guidelines-Revision1.pdf (2007). Accessed 11 August 2018
2. Slater, D., Ridenoure, R., Klumpar, D., Carrico, J., Jah, M.: Light to Sound: The Remote Acoustic Sensing Satellite (RASSat). In: 30th Annual AIAA/USU Conference on Small Satellites, Logan, Utah (2016)
3. Bell, A.G.: On the Production and Reproduction of Sound by Light. *Am. J. Sci. Third Series.* **20**(118), 305–324 (Oct. 1880)
4. Davis, A., et al.: The Visual Microphone: Passive Recovery of Sound from Video. *ACM Trans. Graphics.* **33**(4), Article No. 79
5. Gurnett, D.A., Kurth, W.S., Burlaga, L.F., Ness, N.F.: In Situ Observations of Interstellar Plasma with Voyager 1. *Science.* **341**, 1489–1492 (2013). <https://doi.org/10.1126/science.1241681>
6. Jain, A., Ross, A., Prabhakar, S.: An Introduction to Biometric Recognition. *IEEE Trans. Circuits Syst. Video Technol.* **1**, 14 (2004)
7. Adeoye, O.: A Survey of Emerging Biometric Technologies. *Int. J. Comput. Appl.* **10**, 9 (2010)
8. Kelec, T., Jah, M.: Detection and orbit determination of a satellite executing low thrust maneuvers. *Acta Astronaut.* **66**, 798–809 (2010)
9. Aaron, B.S., “Geosynchronous satellite maneuver detection and orbit recovery using ground based optical tracking.” Masters Thesis, Massachusetts Institute of Technology, (2006), <http://hdl.handle.net/1721.1/36175>
10. Wetterer, C.J., Jah, M.: Attitude Estimation from Light Curves. *J. Guid. Control Dynam.* **32**(5), 1648–1651 (2009)
11. Haugse, E. D., Juengst, C. D., Salus, W. L., and Lollock, J. A., “On orbit system identification,” Structural Dynamics and Materials Conference and Exhibit, 37th, Salt Lake City, UT, Apr. 15–17, (1996), Technical Papers. Pt. 4. (A96–26801 06–39)
12. Oda, M., Hagiwara, Y., Suzuki, S., Nakamura, T., Inaba, N., Sawada, H., Yoshii, M., Goto, N.: Measurement of Satellite Solar Array Panel Vibrations Caused by Thermal Snap and Gas Jet Thruster Firing (2011). <https://doi.org/10.5772/22034>
13. Herber, D., McDonald, J., Alvarez-Salazar, O., Krishnan, G., and Allison, J. . Reducing Spacecraft Jitter During Satellite Reorientation Maneuvers via Solar Array Dynamics. AIAA AVIATION 2014 -15th AIAA/ISSMO Multidisciplinary Analysis and Optimization Conference. (2014) <https://doi.org/10.2514/6.2014-3278>
14. Bae, S.K., Choi, B., Chung, H., Shin, S., Song, H., Seo, J.H.: Characterizing microscale aluminum composite layer properties on silicon solar cells with hybrid 3D scanning force measurements. *Sci. Rep.* **6**, 22752 (2016). <https://doi.org/10.1038/srep22752>
15. Spurbeck, J.A., “Near Real Time Satellite Event Detection, Characterization, and Operational Assessment via the Exploitation of Remote Photoacoustic Signatures.” Masters Thesis, The University of Texas at Austin, (2019), <https://doi.org/10.26153/tsw/2220>

16. Nicolls, M., Vittaldev, V., Ceperley, D., Creus-Costa, J., Foster, C., Griffith, N., Lu, E., Mason, J., Park, I.K., Rosner, C., and Stepan, L. "Conjunction Assessment For Commercial Satellite Constellations Using Commercial Radar Data Sources", Advanced Maui Optical and Space Surveillance Technologies Conference, (2017)
17. Archuleta, A. and Nicolls, M. "Space Debris Mapping Services for use by LEO Satellite Operators", Advanced Maui Optical and Space Surveillance Technologies Conference, (2018)
18. Mallik, V., Jah, M.K.: Reconciling space object observed and solar pressure albedo-areas via astrometric and photometric data fusion. *Adv. Space Res.* (2018) <https://doi.org/10.1016/j.asr.2018.08.005>
19. Frigo, M., Johnson, S.G.: The Design and Implementation of FFTW3. *Proc. IEEE.* **93**(2), 216–231 (2005) Invited paper, Special Issue on Program Generation, Optimization, and Platform Adaptation

Publisher's Note Springer Nature remains neutral with regard to jurisdictional claims in published maps and institutional affiliations.

Affiliations

Justin Spurbeck¹ · Moriba K. Jah¹ · Daniel Kucharski² · James C. S. Bennett³ · James G. Webb⁴

✉ Justin Spurbeck
jspurbeck@utexas.edu

Moriba K. Jah
moriba@utexas.edu

- ¹ Aerospace Engineering and Engineering Mechanics Department, Cockrell School of Engineering, The University of Texas at Austin, Austin, TX 78712, USA
- ² Research Fellow, Space Environment Research Centre, SERC, Canberra, Australia. Visiting Researcher, Institute for Computational Engineering and Sciences, The University of Texas at Austin, Austin, TX 78712, USA
- ³ Astrodynamics Group Leader, EOS Space Systems Pty Ltd, Queanbeyan, Australia. Research Program Leader, Space Environment Research Center, Canberra, Australia
- ⁴ Instrument Scientist, EOS Space Systems Pty Ltd, Queanbeyan, Australia